Supporting Information for "Remote Sensing of Pumice Rafts Using Machine-Learning Classification of Multispectral Satellite Images"

Maggie Zheng[1], Tushar Mittal[1], Kristen E. Fauria[2], Ajit Subramaniam[3],

Martin Jutzeler[4]

[1]Department of Earth, Atmospheric and Planetary Sciences, Massachusetts Institute of Technology, Cambridge, Massachusetts, USA

[2]Department of Earth and Environmental Sciences, Vanderbilt University, Nashville, Tennessee, USA

[3]Lamont-Doherty Earth Observatory, Palisades, New York, USA

[4]Centre for Ore Deposit and Earth Sciences (CODES), University of Tasmania, Hobart, Australia

Contents of this file

Supplementary Text

Text S1. - Other Raft Detection Algorithms In addition to ML algorithms, we tried other spectral index or simple rule based algorithms for raft detection. For instance, we set bounded ranges for the measured brightness Sentinel-2 spectral bands, based on our calculated spectral response curves. We found that this algorithm could differentiate between pumice and non-pumice pixels in a single image for a chosen day and time. However, when applied to different geo-temporal areas, this method required significant

adjustment each time for good accuracy. Similarly, we found that an algorithm just using spectral indices to emphasize specific characteristics of the spectra was not as robust as our final ML algorithm.

Text S2. - Raft Morphology In order to assess whether there is any clear visual morphological difference between new vs. older, remobilized pumice rafts, we analyzed the raft morphology compared to rafts from the new 2019 eruption in the Tonga area (Supplement Figure S9, Planet Labs Imagery). The Tonga raft image from September 6, 2019, was taken about a month after the eruption, and shows that the raft has significantly dispersed from its initial shape (See Figure 2A, Jutzeler et al., 2020). Nevertheless, the Tonga rafts are morphologically distinct from the Rabaul rafts (Some images from March-April 2020, Supplement Figure S9). Although both the rafts interact with the ocean eddies and surface wind stresses, only the pumice concentration pattern for only the Tonga rafts have a distinctive sharp trailing edge and a diaper-tail shaped concentrated region. Instead, the Rabaul rafts trend toward longer, more diffusive-type formations with several smaller, disconnected strands. Since the interaction of pumice rafts with ocean and surface wind dynamics is not well-understood (See discussion in Jutzeler et al., 2020), we do not have a clear physical understanding of why these differences occur. We hypothesize that the morphological differences may due to the rounding of pumice particles in re-suspended rafts due to more prolonged exposure to wave motion and/or surface erosion. Additionally, the pumice particle sizes in the re-suspended rafts may differ from the Tonga raft due to either different eruptive dynamics or preferential selection of a certain pumice size class during the re-suspension process. Based on related work on the interaction of buoyant particles (e.g., marine litter, Sargassum) with the ocean eddies

and wind-driven Langmuir circulation (Thorpe, 2004; Van Sebille et al., 2020; Chang et al., 2019; Miron et al., 2020; Beron-Vera, 2020), we expect the differences in shape and size of pumice to have a significant impact on the raft morphology. It is also surprising that the re-rafted pumice remains buoyant for extended periods at the ocean's surface, despite the weathering and erosion. The two potential mechanisms for explaining the long flotation times for pumice rafts, in general, are gas trapping by water within the pumice and gas-filled isolated porosity (Fauria et al., 2017). Since these processes' efficiency is directly related to the pumice micro-structure, a detailed analysis of the re-rafted Rabaul pumice can test if these mechanisms can explain the frequent raft re-suspension in this region.

Text S3. - Detection of Discolored Water While our study focuses primarily on detecting pumice rafts, we included classes for discolored water as another signature for submarine volcanic eruptions. Our algorithm is moderately successful at detecting discolored water, as illustrated by a classified image from the Kavachi submarine volcano (Supplement Fig S1). However, we found that the detection of these classes is more challenging than pumice rafts. Since discolored water physically represents a mixture of hydrothermal fluids/suspended material with seawater, there is less distinction between the spectral characteristics of the discolored and normal water. Additional work potentially using more input features for ML algorithms is required to improve detection accuracy and robustness. For instance, some two/three-band spectral indices can be included as input features (Qi et al., 2020). Although we found that using spectral index alone did not result in a robust classifier, a thorough examination combining spectral indexes and full reflectance data would likely help improve the detection. Additional datasets outside

of Sentinel-2 (e.g., chlorophyll ocean color and fluorescence line heights) can potentially be included to improve the accuracy of the ML algorithm (Whiteside et al., 2021) and distinguish between discolored water and plankton blooms in response to an influx of nutrients (Wilson et al., 2019; Black et al., 2020; Qi et al., 2020; Kritten et al., 2020).

Text S4. - Algorithm Details Since we are interested in developing an algorithm that can be applied to different geo-temporal areas without significant user adjustment, we used Machine Learning (ML) algorithms due to their significant success in image classification (Abburu & Golla, 2015). ML algorithms can be automated, non-linear, iteratively improved, and easily scaled to extensive data collections. This makes them reasonable candidates for our scientific goal of detecting pumice rafts globally. Specifically, we used the GEE-provided Random Forest (RF) classifier to classify the image pixels (Fig 1C). RF classifiers build multiple decision trees, each based on a randomly selected subset of possible input parameters (here spectral bands). Each tree then classifies a pixel based upon its unique set of branches, and finally, a majority vote is passed to decide the final classification for the pixel (Belgiu & Drăguţ, 2016). Our algorithm used an RF classifier with 32 trees since it empirically provided a good, stable classification algorithm and robustness against overfitting. Since the RF algorithm is already implemented in the GEE platform, it is easy to query any Sentinel-2 image and return a classified image. Each class is highlighted in a specified color (See GEE Scripts provided with the manuscript for specific examples).

Text S5. - Algorithm Validation To evaluate method accuracy, we can construct a confusion matrix using a set of validation data. Confusion matrices compare predicted values against the validation or known values and thus are used to calculate performance

metrics for classification algorithms, such as misclassification rate and accuracy. The validation set was constructed by manually demarcating areas of pixels that were not used to train the classifier and labelling each area as the appropriate class. Then, corresponding pixels from the originally classified are sampled and compared to the validation set of pixels. A confusion matrix is constructed based on how many of the classified pixels match the validation pixels. For our main training area in Rabaul on April 20, 2020 (Fig 2B), the confusion matrix returns an accuracy of 0.9164 (Supplementary Figure S11). This indicates that around 91% of the pixels were classified into the same category as our validation set. The high accuracy is a good indicator that our algorithm can automatedly detect and trace rafts.

Text S6. - Sentinel-2 Product The Multi-Spectral Instrument (MSI) onboard Sentinel-2 collects data from 13 different spectral bands at varying resolutions, and GEE offers two different data products for Sentinel-2 — Top-of-Atmosphere and Surface Reflectance. Since the Surface Reflectance collection typically processes the MSI data assuming land reflectance values rather than ocean values, we used the Level-1C Top-of-Atmosphere Reflectance product. We note that Sentinel-2's spectral bands are similar to several other Earth observing satellites, particularly Landsat-8 and Landsat-7. Thus, we anticipate that the methodology and algorithm developed in this study can be transferred to Landsat data products.

Text S7. - Algorithm Application Details Before applying the algorithm, we applied a land mask. As we are focusing only on signatures of underwater eruptions that are found in water, we could disregard every images' land pixels. Thus, we masked the land pixels in the images using data from the Global Surface Water dataset, a high-resolution

dataset that shows the location and spread of surface water from 1984-2015 (Pekel et al., 2016). Using this land mask effectively removed the land pixels from consideration by the algorithm. The land mask could be used in most areas, but it could sometimes not be employed in the Tonga region due to small islands and atolls. We manually filtered the classified image to remove any land pixels misidentified as pumice rafts in these cases. Due to inherent computational limits for GEE accounts, the algorithm was applied to month or half-a-month long intervals of time with sufficient resolution to see where the classifier marked out pumice (see the scripts for examples). After image classification, pumice rafts were identified through manual review of the classified images.

Text S8. - Rabaul Eruption History Since the last caldera forming eruption, the volcanic activity has built up multiple vents encircling the bay, including the historically very active Vulcan and Tavurvur vents (See Figure 3A, large compositional range from basalt to dacite). The low-lying Rabaul caldera's outer flanks are composed of thick tuff from pyroclastic-flows deposited during the caldera-forming Plinian eruptions (GVP, 2006). Since the town of Rabaul is located nearby, volcanic activity in the area is nominally well-recorded. In 1878, twin eruptions of both the Tavurvur and Vulcan vents generated a large pumice raft that was large enough to form an island and cover the neighboring bay (Bernard & Bouvet de Maisonneuve, 2020). In 1937, the early stage of an eruption at Vulcan killed 507 people and built up a cone such that Vulcan island was connected to the mainland (Bernard & Bouvet de Maisonneuve, 2020). Shortly after, Tavurvur also erupted, albeit in a series of smaller events (Bernard & Bouvet de Maisonneuve, 2020). Both vents produced pumices, and the samples from this 1937 twin eruption are extremely similar to those collected from the 1878 eruption (Bernard & Bouvet de

Maisonneuve, 2020). Rabaul also has a history of more recent pumice raft formation. While the eruption in 2006 (Tavurvur vent) produced a small raft and the eruption in 2014 (Tavurvur vent) deposited pumices in the area (Bernard & Bouvet de Maisonneuve, 2020), the last major raft-forming eruption was in 1994 (VEI 4 eruption GVP, 1994b, 1994a, 2006, , a simultaneous eruption from Vulcan and Tavurvur vents). The 1994 large raft from the Vulcan vent covered the bay in front of town of Rabaul, with a maximum thickness of up to $\sim$ 1.5 m (GVP, 1994b). Since the 1994 twin eruption, there has been intermittent semi-continuous activity at the Vulcan and Tavurvur vents, but no activity has been recorded since the 2014 eruption (Tavurvur vent) (Bernard & Bouvet de Maisonneuve, 2020).

Text S9. - Discolored Water Classes Training samples for Discolored Water Type I (shown in turquoise in the classified images) were drawn from the discolored water emanating from around the Tavurvur vent of the Rabaul caldera, likely due to the interaction of hydrothermal fluids with ocean water (Baker et al., 2002). Training samples for Discolored Water Type II (shown in magenta in the classified images) was drawn from a river's mouth to the south of the pumice raft. Consequently, the magenta discolored water class is likely to be more sediment-rich, while the turquoise discolored water class is more likely to indicate the presence of hydrothermal fluids.

Text S10. - Further Opportunities in Other Satellite Products In our study, we have focused on Sentinel-2 due to its high resolution and revisit frequency. Sentinel-2 offers coverage that includes all coastal water extending up to 20 km from the shoreline, all islands with an area greater than 100 square kilometers, and all closed seas (Drusch et al., 2012). Thus, using our algorithm, pumice rafts can be detected globally within Sentinel-

2's coverage areas. With some minor modifications, our new algorithm can be extended to include other satellites, such as Landsat-7/8, ASTER, MODIS, and Sentinel-2. Including these other satellites will allow for greater spatial coverage area, faster revisits, and a longer total duration of available historical imagery. Using GEE as a tool makes this task numerically feasible and more viable for a global-scale analysis.

Text S11. - Further Potential Algorithm Improvements Including additional input features (e.g., spectral ratios, multi-band spectral indices) may help improve the accuracy of the algorithm and make it fully automated. Furthermore, more feature engineering is necessary for robust discolored water detection. This could potentially also include co-located (and close in time) data products from other satellite imagery such as Chl concentration and SST from Sentinel-2 ($\sim$ 300 m/pixel) (e.g., Whiteside et al. 2021). Another potential improvement involves normalizing the affected images based on expected "ocean water" pixels before being passed to the classifier. In addition, GEE offers image metadata, including the satellite's viewing geometry and the area's cloudy percentage data at the time of the image collection. Applying viewing angle and cloudiness bounds outside of which the algorithm fails can filter out un-classifiable images.

In addition, our present ML algorithm only uses pixel scale information for classification and does not use any information from neighboring pixels or physical expectations for the rafts' shapes. This information can be particularly useful when distinguishing between cloud cover and pumice rafts, where our present semi-automated algorithm has the most difficulty. Generally, the shapes of clouds and pumice rafts are significantly distinct from each other. In addition, clouds often occur as repetition of similar shapes, so clouds may be better distinguished with pattern recognition ML algorithms. This could provide a pos-

sible solution to differentiate between these cloud and pumice pixels by adding additional spatial features to the RF algorithms.

Text S12 - Planet Imagery Planet Labs offers very high resolution imagery (∼3m/pixel) of the entire Earth with a very frequent revisit time (daily). While we use this high resolution imagery to more closely examine images of the rafts that our algorithm detects, we primarily focus on using GEE resources for our study, as very high resolution imagery (e.g., Planet Labs) is typically not publicly available without commercial licenses.

Text S13 - Puyehue-Cordón Caulle Rafts We compared the spectral response curves to those of pumice rafts floating in lakes near the Puyehue-Cordón Caulle volcano complex, located in Chile (Elser et al., 2015). These lake rafts were formed from a higher silica eruption than the ones likely to have produced the rafts in the Tonga and Rabaul regions. Sentinel-2 images were not available for the Puyehue-Cordón Caulle lake rafts, so Landsat 8 images were used instead. Landsat 8 does not have as fine coverage as Sentinel-2, so not all of the same wavelengths were available. We find that the spectra for the lake pumice is broadly consistent with the shape of the other rafts.

Text S14 - Use of Landsat and Planet Imagery: Other Eruption Signatures We manually checked each day our algorithm detected a raft, as well as surrounding days with lower resolution (Landsat 7, Landsat 8) as well as higher resolution imagery (Planet Labs), to check if the rafts are associated with any other eruptive signatures expected for shallow submarine eruptions (e.g., aerial plumes, discolored water). We did not find signatures of eruptions such as aerial plumes or ash fall. Although there was some discolored water (indicator of hydrothermal fluid mixing) around the volcano vent, we did not find a significant relationship between the raft's spatial location and discolored water,

or between the spatial area of discolored water (as a proxy for hydrothermal activity intensity) and the size of the raft (Supplement Fig S8). In addition, we did not find any significant shallow seismic activity near the Rabaul area co-incident with raft detection (Bondár & Storchak, 2011). Thus, we interpret that the detected rafts are not actually products from a new submarine eruption.

Text S15 - Use of Landsat Imagery: Rabaul Raft Detections Outside of Sentinel II Coverage Period To examine whether the more sparse raft detections in the Rabaul area prior to 2018 was due to the precipitation history or the lower satellite coverage prior to the launch of the second Sentinel II, we used Landsat 7 and Landsat 8 imagery to assess images before 2018 (Hartpence, 2021; Goward et al., 2001; Roy et al., 2014). Landsat 7 and Landsat 8 offer lower resolution (30 m/pixel) and longer daily revisit frequency ($>$ 16 days). However, Landsat 7 and Landsat 8 have been active since 1999. From manually analyzing series of Landsat images from the pre-Sentinel period, we found only a few raft images. Thus, we cannot say definitively whether the spike in raft detections using our algorithm starting in 2018 is more likely due to the increase in coverage after the second Sentinel-2 satellite launch rather than long-term precipitation patterns.

Supplementary Figures

- SM1 : Kavachi Submarine Eruption Classification, River Plume Classification, Classification of 2nd Tonga 2019 raft image.
- SM2 : Daily precipitation, Wind velocity magnitude, and mean air temperature against Sentinel-2 pumice raft detection.

• SM3 : Daily precipitation, Wind velocity magnitude, and mean air temperature probability distributions for raft vs non-raft detection days in Sentinel-2 raft detection.

• SM4 : Comparison of pumice spectral response curves in both Rabaul and Tonga for various dates .

• SM5 : Comparison of high resolution Planet imagery for Tonga rafts and Rabaul rafts (See Supplementary Data Material for additional imagery)

• SM6 : RGB and classified images of Anak Krakatau

• SM7 : Classification algorithm confusion matrix

• SM8 : Comparison of Pumice Raft Detection (Yes/No) and hydorthermal activity (Discolored water category, larger values for more activity in the Tavurvur vent region) for Planet Labs detection. Note the lack of relation between the hydrothermal activity and likelihood of detecting a raft in a non-cloudy image.

• SM9 : Examples of high hydrothermal activity in the Tavurvur vent region (Planet Labs Imagery).

• SM10 : Comparison of using the Top-of-Atmosphere (Level-1C) vs. the atmospherically corrected Surface Reflectance (Level-2A) Sentinel-2 data products with our algorithm to detect a raft in the Tonga region on 09/29/2019

Additional data analysis figures for different rolling windows (3,5,7,9 days) - mean, sum, standard deviation - as well as data shifts (comparing climate parameters 3,5,7,9 days before the raft sighting) are provided in the Supplementary Data file as well as on the Figshare file. We also provide the python notebooks for the analysis to allow easy analysis for additional data windows.

GEE Script Links Script Links (also provided with Figshare as a static copy) :

• Spectral Curves– plots the mean and standard deviation of spectral response curves, https://code.earthengine.google.com/878027cf43a77bae30bbacaf072e5451

• Classifier– runs classification on either single images or filmstrips of multiple days, https://code.earthengine.google.com/e63e4ea41701db7ea9d26cf6f54b5ecd

• Climate Time Series– collects climate data (precipitation, wind, temp., etc.) over extended time period and generates plots https://code.earthengine.google.com/e5fe72a393e61a0bd56e286751a64a59

Figshare Link Static copy of the script links:

• https://figshare.com/projects/Pumice_Raft_Detection_Using_Machine-Learning_on_Multispectral_Satellite_Imagery/126466

References

Abburu, S., & Golla, S. B. (2015). Satellite image classification methods and techniques: A review. *International journal of computer applications*, *119*(8).

Baker, E. T., Massoth, G. J., de Ronde, C. E., Lupton, J. E., & McInnes, B. I. (2002). Observations and sampling of an ongoing subsurface eruption of kavachi volcano, solomon islands, may 2000. *Geology*, *30*(11), 975–978.

Belgiu, M., & Drăguţ, L. (2016). Random forest in remote sensing: A review of applications and future directions. *ISPRS journal of photogrammetry and remote sensing*, *114*, 24–31.

Bernard, O., & Bouvet de Maisonneuve, C. (2020). Controls on eruption style at rabaul, papua new guinea – insights from microlites, porosity and permeability measurements. *Journal of Volcanology and Geothermal Research*, *406*,

107068. Retrieved from https://www.sciencedirect.com/science/article/pii/S0377027320303346 doi: https://doi.org/10.1016/j.jvolgeores.2020.107068

Beron-Vera, F. J. (2020). Nonlinear dynamics of inertial particles in the ocean: From drifters and floats to marine debris and sargassum. *Nonlinear Dynamics*, 1–26.

Black, B., Mittal, T., Lingo, F., Walowski, K., & Hernandez, A. (2020). Assessing the environmental consequences of the generation and alteration of mafic volcaniclastic deposits during large igneous province emplacement. *Large Igneous Provinces: A Driver of Global Environmental and Biotic Changes*, 117–131.

Bondár, I., & Storchak, D. (2011). Improved location procedures at the international seismological centre. *Geophysical Journal International*, *186*(3), 1220–1244.

Chang, H., Huntley, H. S., Jr, A. K., Carlson, D. F., Mensa, J. A., Mehta, S., ... others (2019). Small-scale dispersion in the presence of langmuir circulation. *Journal of Physical Oceanography*, *49*(12), 3069–3085.

Drusch, M., Del Bello, U., Carlier, S., Colin, O., Fernandez, V., Gascon, F., ... others (2012). Sentinel-2: Esa's optical high-resolution mission for gmes operational services. *Remote sensing of Environment*, *120*, 25–36.

Elser, J. J., Bastidas Navarro, M., Corman, J. R., Emick, H., Kellom, M., Laspoumaderes, C., ... Modenutti, B. (2015). Community structure and biogeochemical impacts of microbial life on floating pumice. *Applied and Environmental Microbiology*, *81*(5), 1542-1549.

Fauria, K. E., Manga, M., & Wei, Z. (2017). Trapped bubbles keep pumice afloat and gas diffusion makes pumice sink. *Earth and Planetary Science Letters*, *460*, 50–59.

Goward, S. N., Masek, J. G., Williams, D. L., Irons, J. R., & Thompson, R. (2001). The

landsat 7 mission: Terrestrial research and applications for the 21st century. *Remote Sensing of Environment*, *78*(1-2), 3–12.

GVP. (1994a). *Report on rabaul (papua new guinea) (wunderman, r., ed.), bulletin of the global volcanism network, 19:10. smithsonian institution.* https://doi.org/10.5479/si.GVP.BGVN199408-252140. (Downloaded : 1st Feb 2021)

GVP. (1994b). *Report on rabaul (papua new guinea) (wunderman, r., ed.), bulletin of the global volcanism network, 19:8. smithsonian institution.* https://doi.org/10.5479/si.GVP.BGVN199408-252140. (Downloaded : 1st Feb 2021)

GVP. (2006). *Report on rabaul (papua new guinea) (wunderman, r., ed.), bulletin of the global volcanism network, 31:9. smithsonian institution.* https://doi.org/10.5479/si.GVP.BGVN200609-252140. (Downloaded : 1st Feb 2021)

Hartpence, A. (2021). *Landsat collection 2* (Tech. Rep.). US Geological Survey.

Jutzeler, M., Marsh, R., van Sebille, E., Mittal, T., Carey, R. J., Fauria, K. E., ... McPhie, J. (2020). Ongoing dispersal of the 7 august 2019 pumice raft from the tonga arc in the southwestern pacific ocean. *Geophysical Research Letters*, *47*(5), e1701121.

Kritten, L., Preusker, R., & Fischer, J. (2020). A new retrieval of sun-induced chlorophyll fluorescence in water from ocean colour measurements applied on olci l-1b and l-2. *Remote Sensing*, *12*(23), 3949.

Miron, P., Olascoaga, M., Beron-Vera, F., Putman, N., Triñanes, J., Lumpkin, R., & Goni, G. (2020). Clustering of marine-debris-and sargassum-like drifters explained by inertial particle dynamics. *Geophysical Research Letters*, *47*(19), e2020GL089874.

Pekel, J.-F., Cottam, A., Gorelick, N., & Belward, A. S. (2016). High-resolution mapping

of global surface water and its long-term changes. *Nature*, *540*(7633), 418–422.

Qi, L., Hu, C., Mikelsons, K., Wang, M., Lance, V., Sun, S., ... Van der Zande, D. (2020). In search of floating algae and other organisms in global oceans and lakes. *Remote Sensing of Environment*, *239*, 111659.

Roy, D. P., Wulder, M. A., Loveland, T. R., Woodcock, C. E., Allen, R. G., Anderson, M. C., ... others (2014). Landsat-8: Science and product vision for terrestrial global change research. *Remote sensing of Environment*, *145*, 154–172.

Thorpe, S. (2004). Langmuir circulation. *Annu. Rev. Fluid Mech.*, *36*, 55–79.

Van Sebille, E., Aliani, S., Law, K. L., Maximenko, N., Alsina, J. M., Bagaev, A., ... others (2020). The physical oceanography of the transport of floating marine debris. *Environmental Research Letters*, *15*(2), 023003.

Whiteside, A., Dupouy, C., Singh, A., Frouin, R., Menkes, C., & Lefèvre, J. (2021). Automatic detection of optical signatures within and around floating tonga-fiji pumice rafts using modis, viirs, and olci satellite sensors. *Remote Sensing*, *13*(3), 501.

Wilson, S. T., Hawco, N. J., Armbrust, E. V., Barone, B., Björkman, K. M., Boysen, A. K., ... others (2019). Kīlauea lava fuels phytoplankton bloom in the north pacific ocean. *Science*, *365*(6457), 1040–1044.

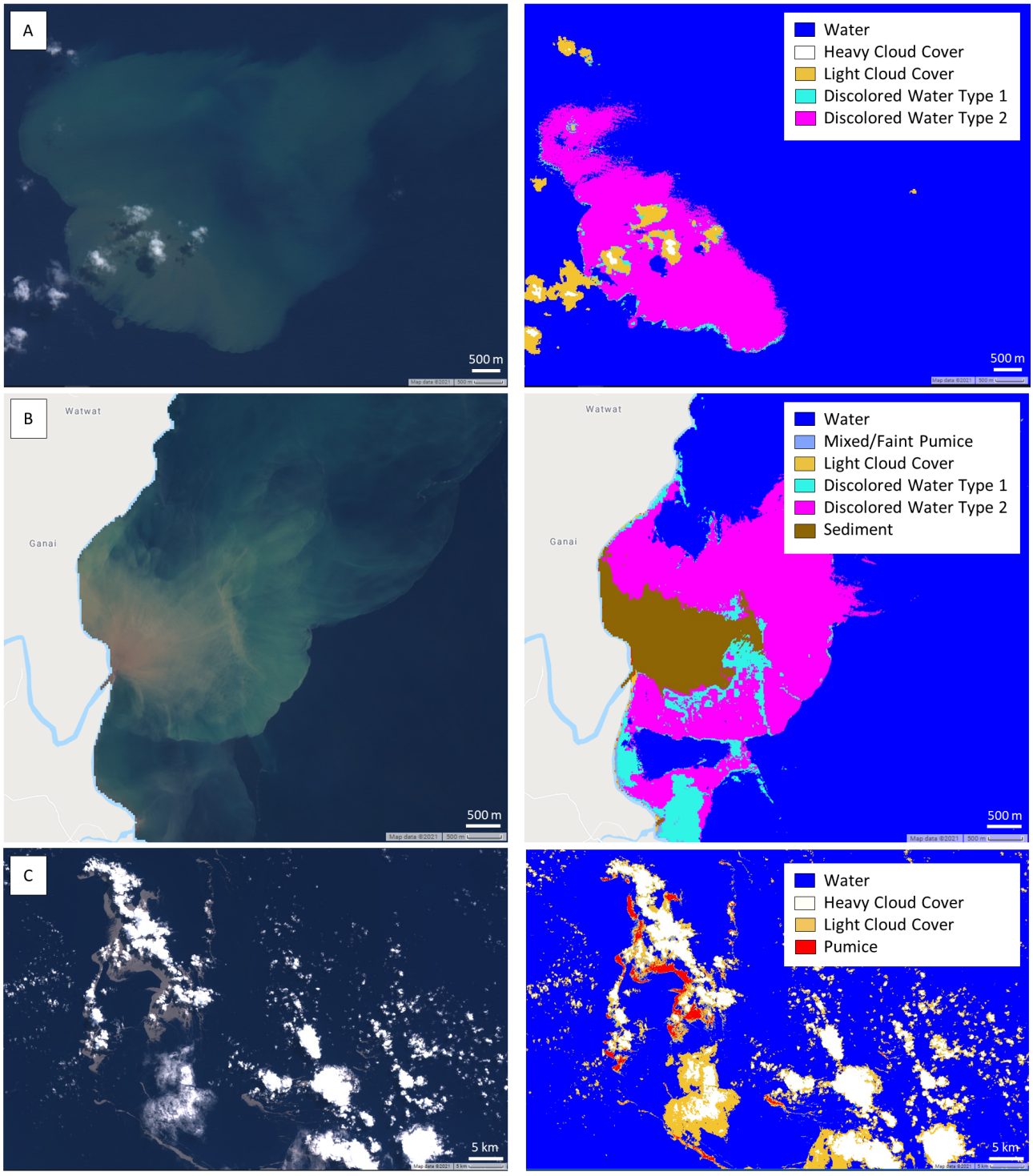

Figure S1. (A) RGB and classified images of Kavachi on 04/24/2020 (B) RGB and classified images of the river delta near Rabaul for 04/20/2020 (C) RGB and classified images for Tonga on 08/16/19

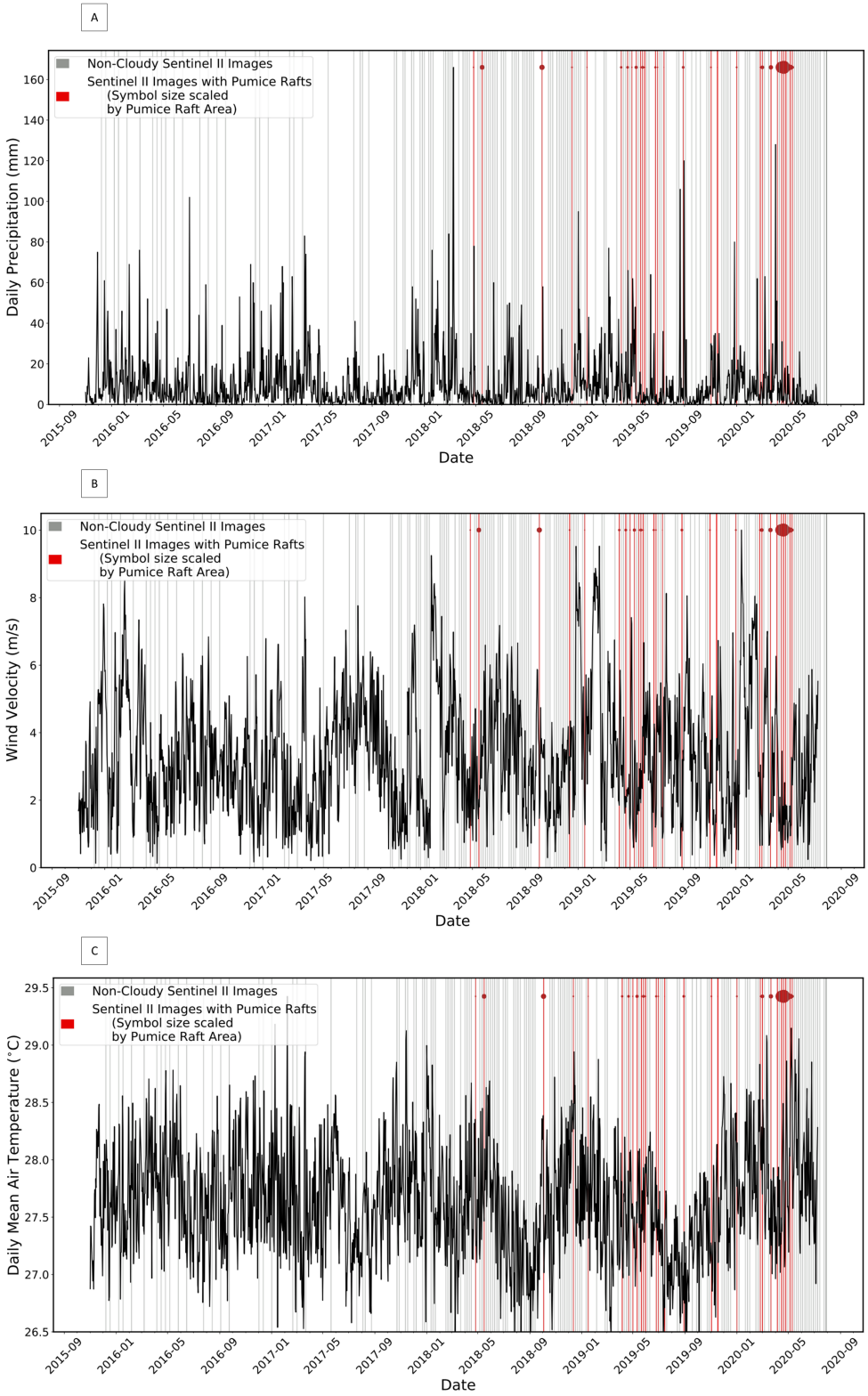

Figure S2. (A) Daily precipitation in Rabaul against Sentinel-2 raft detections (B) Daily wind velocity in Rabaul against Sentinel-2 raft detections (C) Daily mean air temperature in Rabaul against Sentinel-2 raft detections

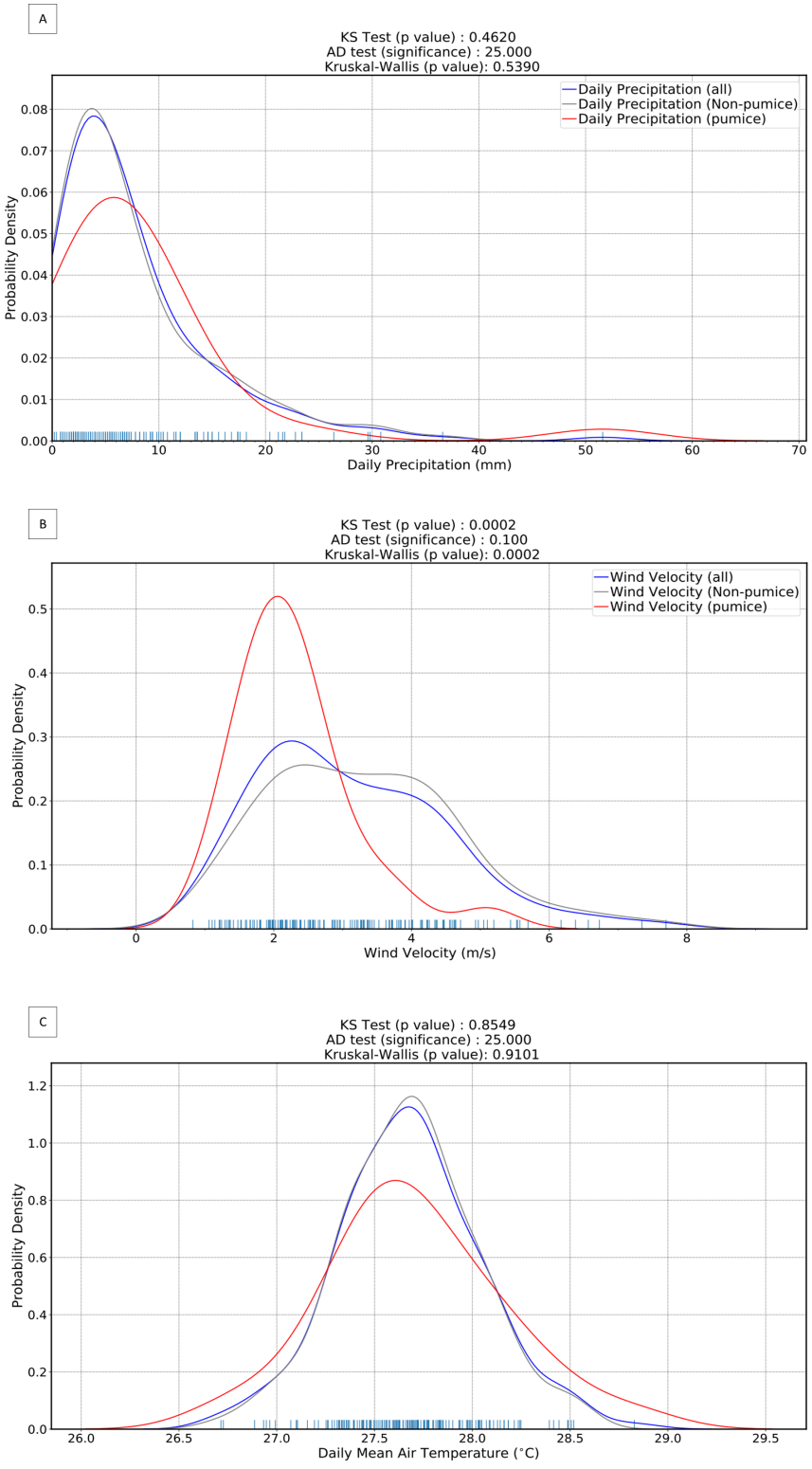

Figure S3. (A) Daily precipitation pdf in Rabaul (5 day rolling window) (B) Daily wind pdf in Rabaul (5 day rolling window) (C) Daily mean air temperature pdf in Rabaul (5 day rolling window)

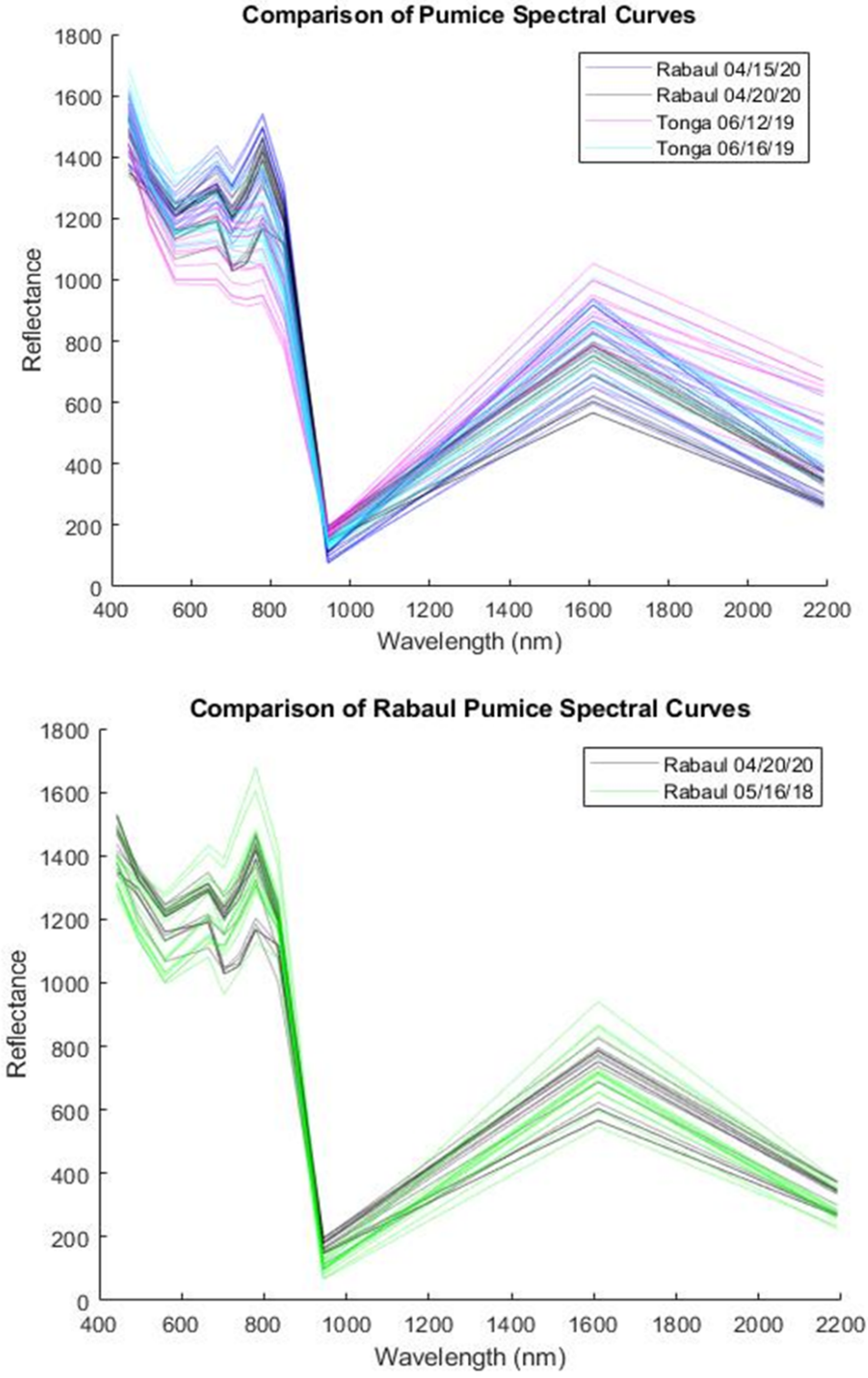

Figure S4. Comparison of pumice spectral response curves in both Rabaul and Tonga for various dates

Figure S5. Comparison of high resolution Planet Labs imagery for Tonga 2019 rafts and newly detected Rabaul rafts - These images provide examples of different raft morphologies.

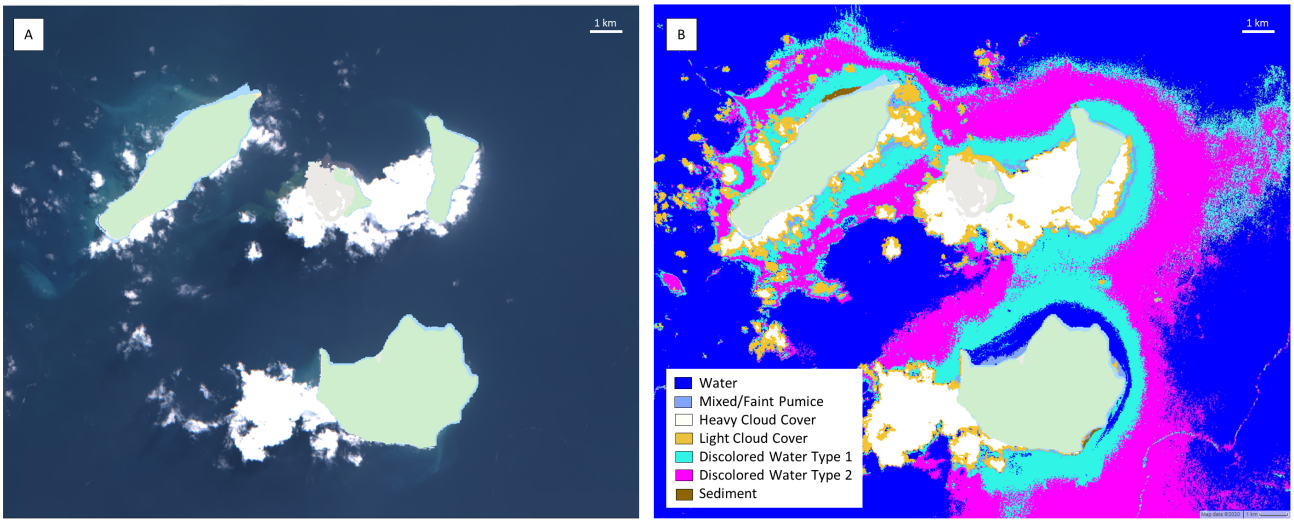

Figure S6. (A) RGB image of Anak Krakatau on 04/15/2019 (B) Classified image of Anak Krakatau on 04/15/2019

	Pumice	Water	Light Clouds	Discolored Water Type 1	Discolored Water Type 2	Sediment	Mixed Pumice	Heavy Clouds
Pumice	408	0	0	0	0	0	0	0
Water	0	1982	83	0	0	0	0	0
Light Clouds	0	0	1029	0	0	0	0	6
Discolored Water Type 1	0	0	0	0	0	0	0	0
Discolored Water Type 2	0	61	0	220	275	0	0	0
Sediment	0	0	0	0	0	78	0	0
Mixed Pumice	0	0	0	0	0	0	2	0
Heavy Clouds	0	0	0	0	0	0	0	281

Figure S7. Classification algorithm confusion matrix

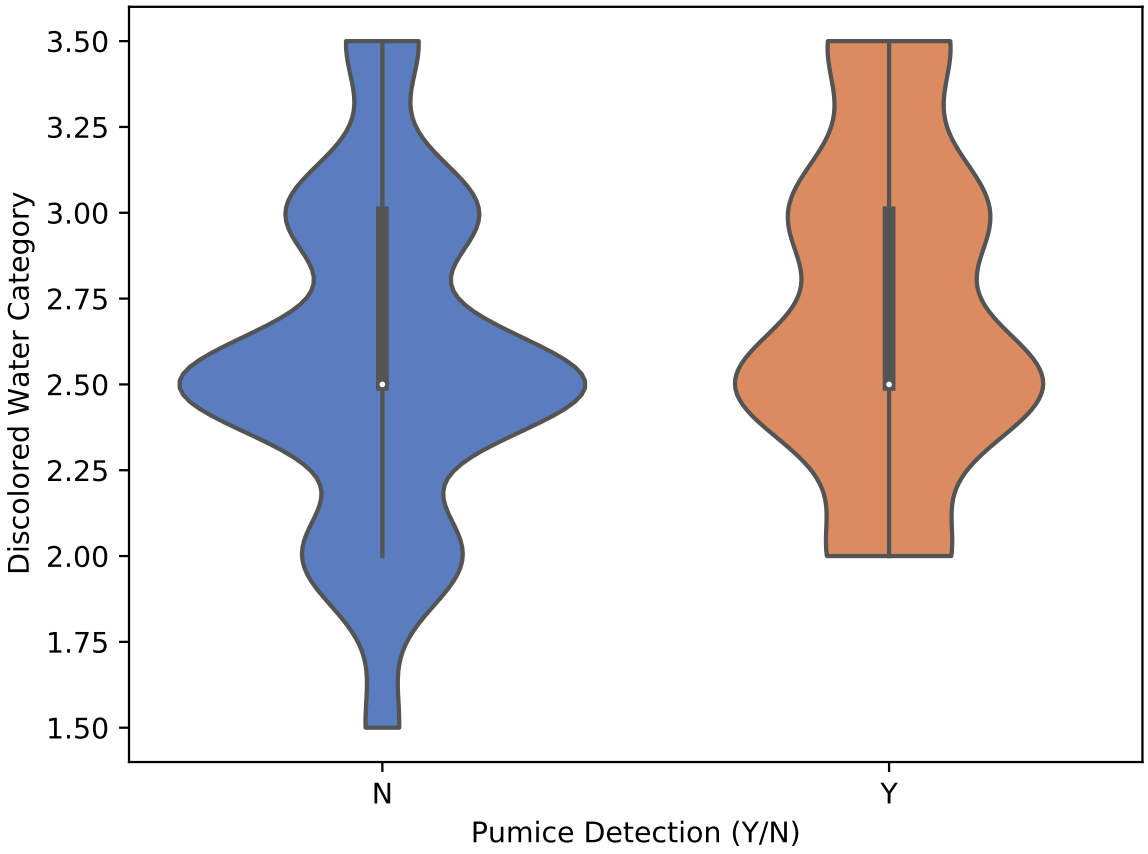

Figure S8. Comparison of pumice raft detection (Yes/No) and hydrothermal activity (discolored water category, larger values for more activity in the Tavurvur vent region) for Planet Labs detection. Note the lack of relation between the hydrothermal activity and likelihood of detecting a raft in a non-cloudy image

Figure S9. Examples of high hydrothermal activity in the Tavurvur vent region (Planet Labs Imagery) (A) 03/09/2011 (B) 09/19/16 (C) 01/07/18

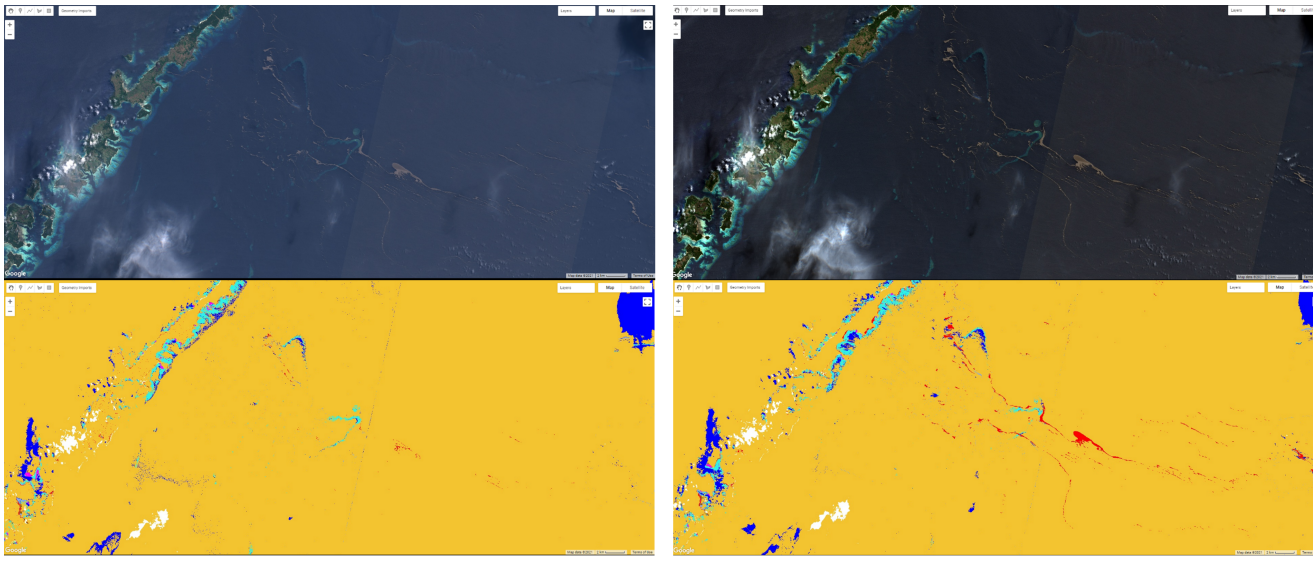

Figure S10. Comparison of using the Top-of-Atmosphere (Level-1C) vs. the atmospherically corrected Surface Reflectance (Level-2A) Sentinel-2 data products with our algorithm to detect a raft in the Tonga region on 09/29/2019

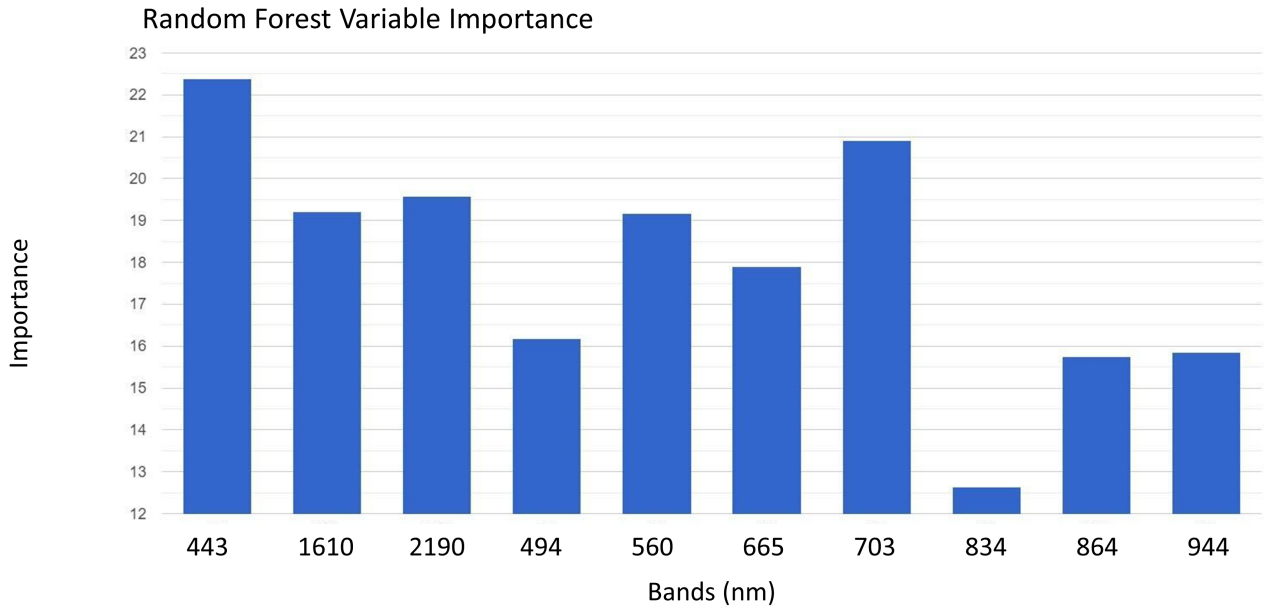

Figure S11. Importance of each Sentinel-2 band in the Random Forest algorithm. This is derived from the summed decrease in Gini impurity index for each individual over all of the trees in the RF classifier. The Gini impurity index is a measure of the probability of an observation being misclassified if it was randomly assigned to a class. The Gini index based estimate of variable importance typically provides a similar importance score for a variable's importance in classification compared to the more numerically intensive approach of permutation importance measure.